Report

Cell Reports

Cofilin-Mediated Actin Stress Response Is Maladaptive in Heat-Stressed Embryos

Graphical Abstract

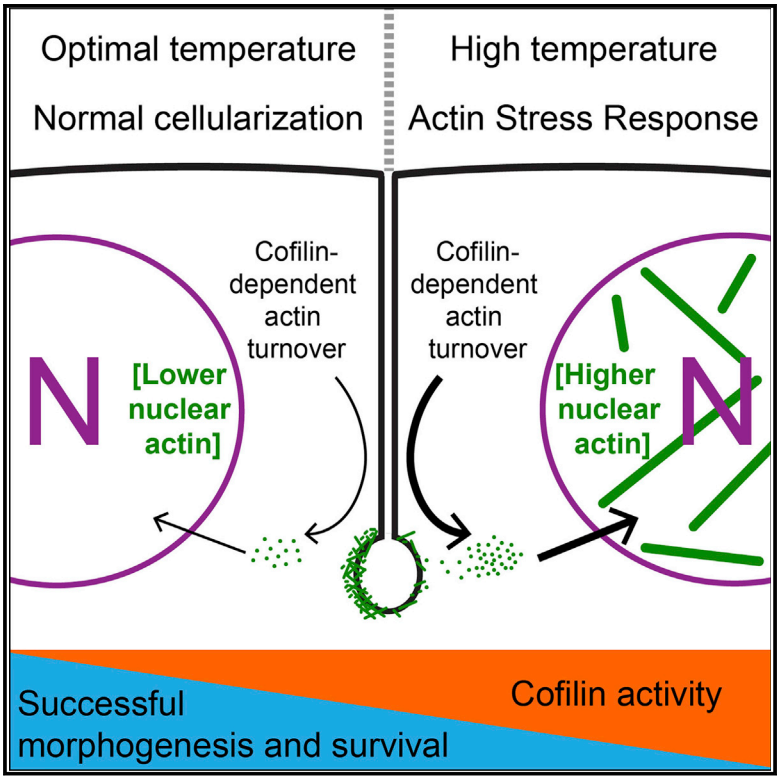

Highlights

- *Drosophila* embryos mount an actin stress response (ASR) against heat stress
- Cofilin mediates the ASR, affecting actin in both the nucleus and the cytoplasm
- In nuclei, actin rods assemble; in cytoplasm, F-actin structures are destabilized
- F-actin destabilization disrupts morphogenesis, and embryo ASR is overall maladaptive

Authors

Lauren Figard, Liuliu Zheng, Natalie Biel, ..., Seth Coleman, Ido Golding, Anna Marie Sokac

Correspondence

sokac@bcm.edu

In Brief

Figard et al. show that heat stress induces an actin stress response (ASR) in early *Drosophila* embryos. This ASR is mediated by a heat-induced increase in Cofilin activity. Increased Cofilin activity destabilizes F-actin structures required for morphogenesis. In addition, the Cofilin-mediated ASR reduces embryo viability.

Figard et al., 2019, Cell Reports *26*, 3493–3501
March 26, 2019
https://doi.org/10.1016/j.celrep.2019.02.092

CellPress

Cell Reports
Report

Cofilin-Mediated Actin Stress Response Is Maladaptive in Heat-Stressed Embryos

Lauren Figard,[1,7] Liuliu Zheng,[1,7] Natalie Biel,[1,2] Zenghui Xue,[1] Hasan Seede,[1,3] Seth Coleman,[1,4,5] Ido Golding,[1,4,6] and Anna Marie Sokac[1,8,*]
[1]Verna & Marrs McLean Department of Biochemistry and Molecular Biology, Baylor College of Medicine, Houston, TX 77030, USA
[2]Integrative Molecular and Biomedical Sciences Graduate Program, Baylor College of Medicine, Houston, TX 77030, USA
[3]Department of Biochemistry and Cell Biology, Rice University, Houston, TX 77005, USA
[4]Center for Theoretical Biological Physics, Rice University, Houston, TX 77005, USA
[5]Applied Physics Graduate Program, Rice University, Houston, TX 77005, USA
[6]Center for the Physics of Living Cells, University of Illinois at Urbana-Champaign, Urbana, IL 61801, USA
[7]These authors contributed equally
[8]Lead Contact
*Correspondence: sokac@bcm.edu
https://doi.org/10.1016/j.celrep.2019.02.092

SUMMARY

Environmental stress threatens the fidelity of embryonic morphogenesis. Heat, for example, is a teratogen. Yet how heat affects morphogenesis is poorly understood. Here, we identify a heat-inducible actin stress response (ASR) in *Drosophila* embryos that is mediated by the activation of the actin regulator Cofilin. Similar to ASR in adult mammalian cells, heat stress in fly embryos triggers the assembly of intra-nuclear actin rods. Rods measure up to a few microns in length, and their assembly depends on elevated free nuclear actin concentration and Cofilin. Outside the nucleus, heat stress causes Cofilin-dependent destabilization of filamentous actin (F-actin) in actomyosin networks required for morphogenesis. F-actin destabilization increases the chance of morphogenesis mistakes. Blocking the ASR by reducing Cofilin dosage improves the viability of heat-stressed embryos. However, improved viability correlates with restoring F-actin stability, not rescuing morphogenesis. Thus, ASR endangers embryos, perhaps by shifting actin from cytoplasmic filaments to an elevated nuclear pool.

INTRODUCTION

Environmental stress significantly challenges developing embryos. In humans, prenatal exposure to hypoxia, drugs, pathogens, or high temperature is associated with increased risk of fetal death or physical malformations and/or defects following birth (Edwards, 2006; Dixon et al., 2011; Hamdoun and Epel, 2007). Environmental stress disrupts cellular function in embryos by generating reactive oxygen species, altering gene expression, inducing apoptosis and heterochronicity, and disrupting signaling networks (Parman et al., 1999; Puscheck et al., 2015; Salilew-Wondim et al., 2014; Crews et al., 2016). Whether these stress-induced disruptions impinge on the actin cytoskeleton, the ultimate architectural driver of embryonic morphogenesis, remains unknown.

Recently, the actin cytoskeleton itself has emerged as a mediator of stress response (Amberg et al., 2012; Baird et al., 2014; Bernstein et al., 2006; Chambers et al., 2015; Higuchi et al., 2013). Many cell types, including neurons, myocytes, and epithelial cells, reorganize their F-actin upon exposure to heat or oxidative stress as part of an inducible actin stress response (ASR; reviewed in Bamburg and Bernstein [2016]; Kanellos and Frame [2016]; Munsie and Truant [2012]). This F-actin reorganization is typified by the assembly of actin "rods" in the nucleus or cytoplasm of affected cells (Ashworth et al., 2003; Iida et al., 1986; Minamide et al., 2000; Ono et al., 1993; Sanger et al., 1980; Vandebrouck et al., 2010). In transiently stressed neuronal cells, rod assembly promotes increased cell survival through an unknown mechanism (Bernstein et al., 2006; Munsie et al., 2012). However, the full extent of the ASR's protective value is still undefined in most cells and is likely to be context dependent.

So far, the ASR has not been described in any embryo. What's more, like other inducible stress responses in early embryos, it is unclear whether an ASR would be protective or would adversely divert normal developmental programs (Hamdoun and Epel, 2007). Here, we identify a maladaptive ASR in heat-stressed *Drosophila* embryos. This ASR destabilizes cytoplasmic F-actin structures, compromises cellularization—the first morphogenetic event in fruit fly development—and reduces embryo viability. Intriguingly, reduced viability appears to be more of a consequence of F-actin destabilization than of mild morphogenesis mistakes.

RESULTS

Heat Stress Induces Intra-Nuclear Actin Rod Assembly in Embryos

During cellularization, plasma membrane furrows invaginate synchronously to package ~6,000 nuclei of the syncytial embryo into a sheet of mononucleate epithelial cells that immediately goes on to gastrulate and eventually forms the larva. Furrow invagination depends on assembly of F-actin and Myosin-2 structures at furrow tips (Sokac and Wieschaus, 2008; Figure 1A,

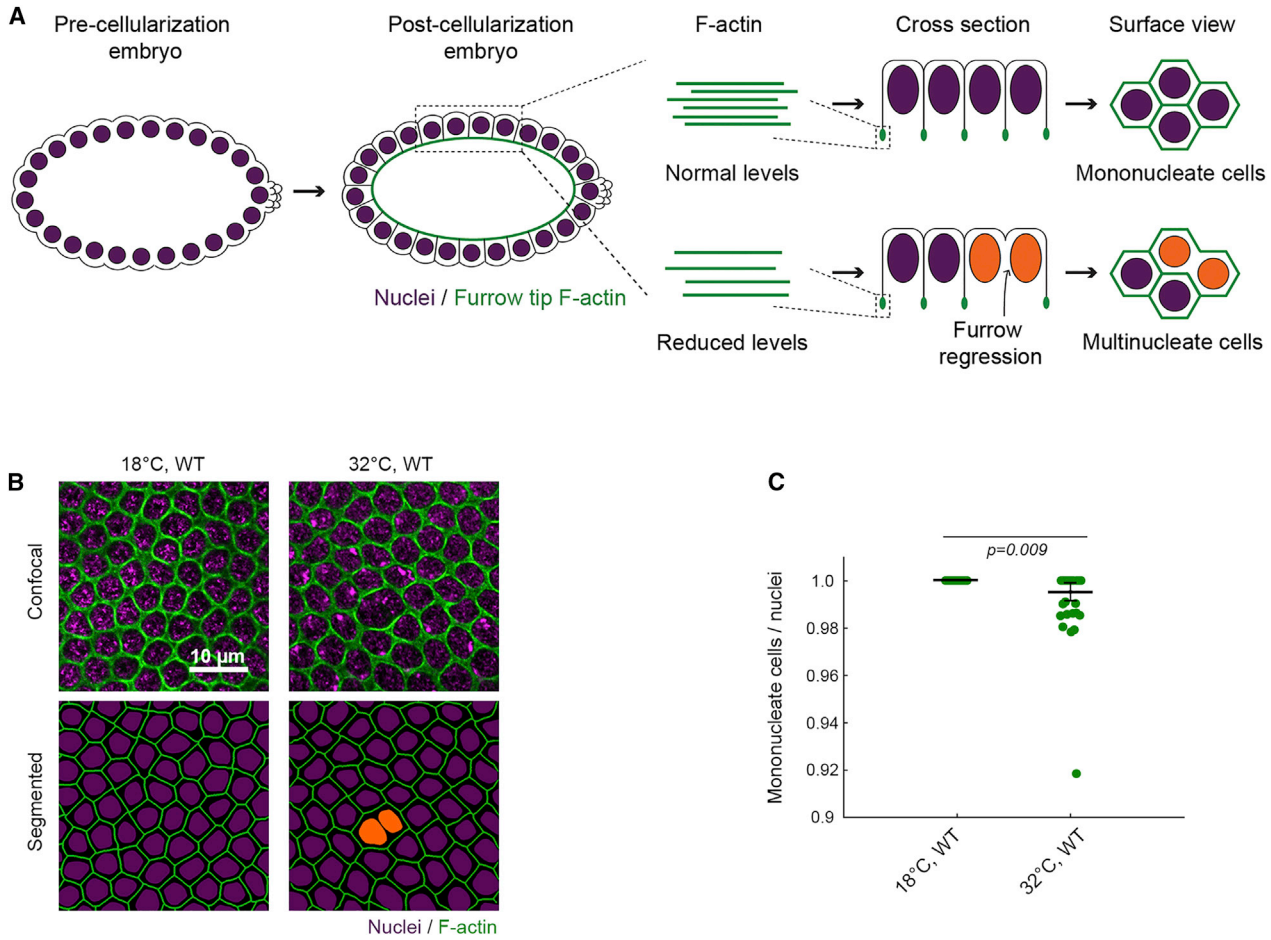

Figure 1. Heat Stress Leads to Cellularization Failures

(A) In embryos with normal levels of F-actin (green), furrows ingress between nuclei (purple) to form mononucleate cells. In embryos with reduced F-actin, some furrows regress, resulting in multinucleate cells (orange nuclei).

(B) Surface views show furrow tip F-actin (phalloidin, green) and nuclei (Hoechst, purple) in wild-type (WT) embryos at indicated temperatures. Multinucleate cells highlighted by orange nuclei in corresponding segmented images.

(C) Severity of multinucleation in embryos at indicated temperatures. Each point represents one embryo (n = 52 embryos per genotype, with ~150 nuclei analyzed per embryo; horizontal lines are means ± SE).

Student's t test used to calculate p value in (C).

cross section). Considered in three dimensions, these furrow tip structures make a hexagonal network across the embryo surface, with each hexagon encircling one nucleus (Figure 1A, surface view). Mutations in positive regulators of F-actin (e.g., Diaphanous/Formin) reduce F-actin levels at all furrow tips and result in the regression of a fraction of furrows (Padash Barmchi et al., 2005; Grosshans et al., 2005; Sokac and Wieschaus, 2008; Zheng et al., 2013). Furrow regressions manifest as multinucleate cells. Thus, multinucleation serves as a proxy for compromised F-actin function during cellularization.

We previously found that wild-type embryos are prone to multinucleation when reared under heat stress (Figures 1B and 1C; Zheng et al., 2013), leading us to hypothesize that F-actin is somehow disrupted by high temperature. To test this hypothesis, we first visualized the actin cytoskeleton in live wild-type embryos injected with rhodamine labeled G-actin (G-actin^{Red}). We chose G-actin^{Red} as a probe, because it readily incorporates into furrow tips during cellularization with no known adverse effects on the process (Cao et al., 2008; Xue and Sokac, 2016). Embryos were injected with G-actin^{Red} at 18°C and then imaged at either 18°C or under heat stress at 32°C (Table S1). This is a mild heat stress, given that standard culturing conditions are 18°C–29°C, and heat shock experiments in *Drosophila* typically use ≥ 37°C (e.g., Bergh and Arking, 1984; Crews et al., 2016). In injected embryos, single plane, confocal surface views captured furrow tip F-actin, as well as cross sections through nuclei. Strikingly, numerous actin rods were seen inside the nuclei of embryos at 32°C (Figures 2A and S1A). These rods resembled actin rods previously associated with the ASR in heat and oxidatively stressed adult cell types (Kanellos and Frame, 2016).

Actin rods in stressed neurons are "stable," meaning there is no actin subunit turnover along their length (Bernstein et al.,

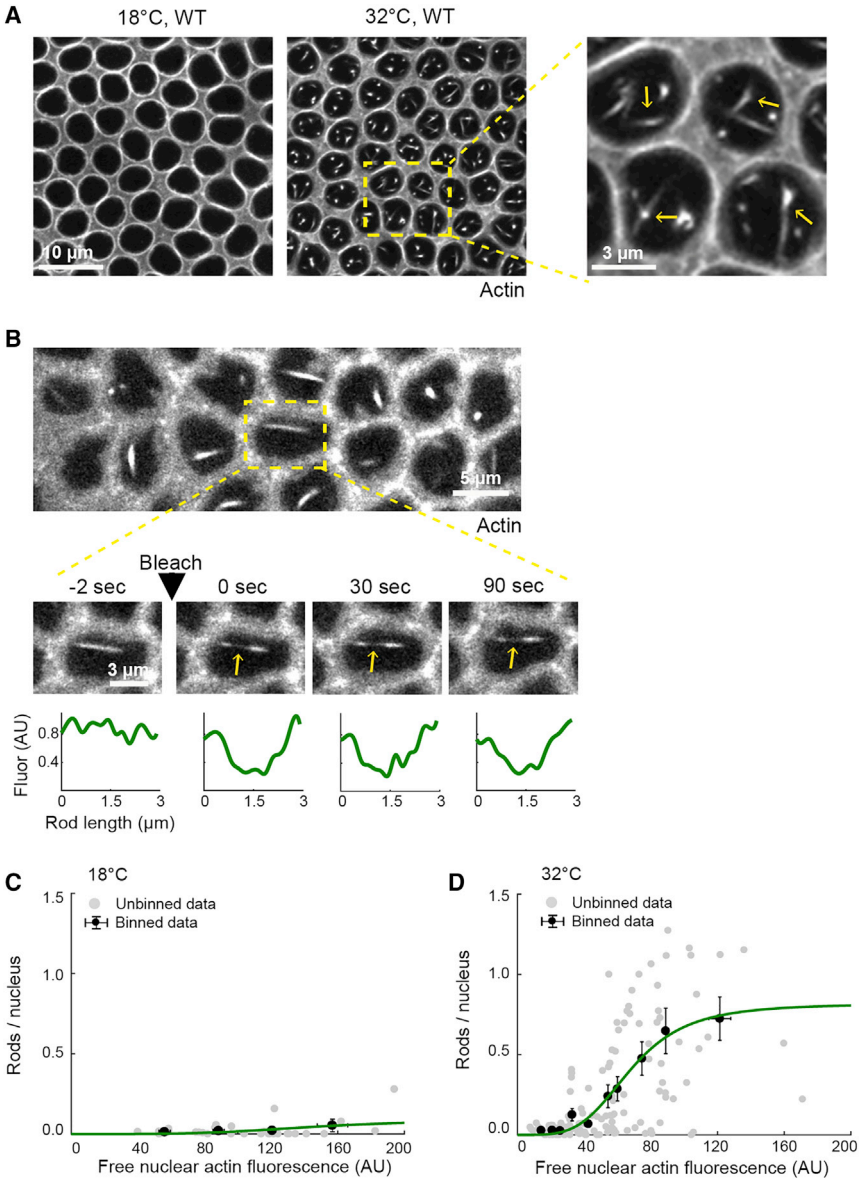

Figure 2. Intra-Nuclear Actin Rods Assemble in Heat-Stressed Embryos

(A) Surface views show G-actin^{Red} in furrow tips in live wild-type (WT) embryos at indicated temperatures. Intra-nuclear rods assemble at 32°C (yellow arrows, higher-magnification inset).

(B) Surface views show FRAP of a rod (G-actin^{Red}) in a WT embryo at 32°C. Higher-magnification time-lapse images show boxed ROI, and yellow arrows indicate bleached mid-section of a rod. FRAP kinetics for that rod plotted below.

(C and D) Rod abundance (rods/nucleus) versus free nuclear actin fluorescence in live WT embryos at 18°C (C) and 32°C (D) ($n \geq 31$ embryos, with rod abundance counted in ≥ 60 nuclei per embryo; free actin fluorescence averaged from three nuclei per embryo). Each gray point represents one embryo, and black points represent binned data (mean ± SE). The green line represents the binned data fitted to a Hill function with Hill coefficient = 4. Related data are shown in Figure S1.

2006; Minamide et al., 2010). To assess subunit turnover in rods in embryos, we measured fluorescence recovery after photobleaching (FRAP) for actin in the central region of rods. Nuclear rods showed no recovery (Figure 2B), whereas F-actin in cytoplasmic furrow tips recovers in tens of seconds (Xue and Sokac, 2016). So, analogous to the ASR in neurons, rods are stable in heat-stressed embryos. Despite this stability, rod assembly is reversible if embryos are shifted back to lower temperature, as previously described for ASR in transiently stressed neurons (Figure S1B; Bamburg and Bernstein, 2016).

We wondered whether intra-nuclear rod assembly depends on free nuclear actin concentration. To probe this dependence, we injected wild-type embryos with a range of G-actin^{Red} concentrations and scored for rod assembly (Figures 2C and 2D). For embryos at 32°C, rod numbers increased with free nuclear actin concentration (Figures 2D). For embryos at 18°C, a few rods formed, but only at ~3-fold higher free nuclear actin level compared to 32°C (Figures 2C and 2D). Thus, rod assembly is concentration dependent at both temperatures, but rods form at lower free actin levels during heat stress. The difference in rod assembly at 18°C versus 32°C was not due to a change in the ratio of free nuclear to free cytoplasmic actin (Figure S1C). Free nuclear and cytoplasmic actin concentrations show the same linear relationship to each other at 18°C and 32°C (Figure S1D), perhaps because embryos are undergoing rapid rounds of mitoses with partial nuclear envelope breakdown. So, regardless of temperature, actin is incorporated into newly reformed nuclei at levels reflecting its free cytoplasmic concentration. Consistent with this, the dependencies between rod assembly and either free nuclear or free cytoplasmic actin concentration were similar (Figures 2C, 2D, S1E, and S1F). Finally, we found a maximum level of free actin in the nucleus that is not exceeded at 32°C, but instead at which additional actin rods are made (Figure S1G). Together, these results support a model where the proportion of free nuclear to free cytoplasmic actin does not change with temperature; however, during heat stress, some additional activity lowers the threshold concentration for actin sequestration in rods.

Cofilin Promotes Actin Rod Assembly in Heat-Stressed Embryos

Next, we asked whether Cofilin provides the activity that promotes rod assembly in heat-stressed embryos. In mammalian cell types, ASR is mediated by stress-induced hyper-activation

of Cofilin, an actin binding protein with diverse functions that influence both cytoplasmic and nuclear actin (Ashworth et al., 2003; Huang et al., 2008; Kim et al., 2009; Minamide et al., 2000; Ohta et al., 1989). Under normal conditions, Cofilin in the cytoplasm binds and severs F-actin to accelerate filament turnover (Andrianantoandro and Pollard, 2006). Cofilin also binds G-actin and works with importins to shuttle free actin into the nucleus (Dopie et al., 2012, 2015). Finally, Cofilin at high concentrations may stabilize F-actin regardless of cellular location (Andrianantoandro and Pollard, 2006; McCullough et al., 2008). During ASR, Cofilin has been shown to promote rod assembly via nuclear import of free actin and/or stabilization of actin rods (Bamburg et al., 2010; Munsie et al., 2012). To then assay Cofilin's role in rod assembly in embryos, we injected G-actin^{Red} into embryos expressing a reduced dose of Cofilin (*cofilin*$^{+/-}$). These embryos express 60.5% ± 3.8% the wild-type level of Cofilin (mean ± SE; n = 4 experiments). Compared to wild-type, *cofilin*$^{+/-}$ embryos were less likely to form rods at 32°C (Figures 3A and 3B), supporting that Cofilin is required for rod assembly in heat-stressed embryos. We did not detect Cofilin in rods, despite trying several fixation protocols and Cofilin antibodies. Instead, given the actin concentration dependence of rod assembly, Cofilin may promote rods by somehow keeping free actin levels high in the cytoplasm and/or nucleus.

Cofilin Upregulation Destabilizes Cytoplasmic F-Actin in Heat-Stressed Embryos

We examined Cofilin's global activity state in whole embryo lysates following heat stress. When Cofilin is dephosphorylated at serine 3 (S3), it can bind G- or F-actin and so is considered active (Bravo-Cordero et al., 2013). Alternatively, when Cofilin is phosphorylated at S3, it cannot bind actin at all and is inactive. We made and validated a polyclonal antibody against *Drosophila melanogaster* Cofilin (*Dm*-Cofilin) that detects both phosphorylated and dephosphorylated Cofilin (top and bottom band, respectively; Figures 3C, S2A, and S2B). Using this antibody, the ratio of phosphorylated to total Cofilin was consistently reduced at 32°C (Figures 3C and 3D), indicating a shift of Cofilin to a higher activity state in heat-stressed embryos. Similarly, we saw a reproducible decrease in levels of phosphorylated Cofilin using a commercially available phospho-specific antibody (P_i-Cofilin; Figure 3C).

Apart from rod assembly, Cofilin's role in F-actin severing predicts that its stress-induced activation would also destabilize normal cytoplasmic F-actin structures (e.g., Ashworth and Molitoris, 1999; Schwartz et al., 1999), and consequently alter the ratio of free to polymer-associated G-actin. In fact, destabilization could generate the free monomer pool that supports rod assembly. However, it is not known whether destabilization of cytoplasmic F-actin is a general feature of ASR. To address this issue, we imaged F-actin levels and dynamics at furrow tips, where Cofilin normally localizes during cellularization (Xue and Sokac, 2016). To quantify F-actin levels, wild-type embryos reared at either 18°C or 32°C were fixed and phalloidin stained in the same tube with internal control embryos reared at 25°C (Histone-GFP; Figure S3). This method avoided tube-to-tube variation in phalloidin staining and allowed normalization to the internal control embryos. We found that heat-stressed embryos have significantly less F-actin at furrow tips (Figures 3E, S3, and S4C). To assay F-actin stability, we performed FRAP using G-actin^{Red} (i.e., faster turnover indicates reduced stability; Mukhina et al., 2007). The half time to recovery for F-actin in furrow tips in wild-type embryos was 19.33 ± 1.15 s at 18°C but sped up to 14.02 ± 0.81 s in embryos at 32°C (Figures 3F and 3G; mean ± SE). No change was seen for the mobile fraction (Figure S4A). These results suggest that the dynamic F-actin in furrow tips is less stable in heat-stressed embryos.

Next, we asked whether Cofilin is driving F-actin destabilization in heat-stressed embryos. In *cofilin*$^{+/-}$ embryos at 32°C, F-actin levels in furrow tips were fully restored to wild-type levels (normalization to Histone-GFP at 32°C; Figures 3H and S4D). Recovery by FRAP slowed to 20.54 ± 1.04 s (mean ± SE), equivalent to the turnover rate in unstressed wild-type embryos (Figure 3G). No change was seen for the mobile fraction (Figure S4B). Notably, F-actin was stabilized in *cofilin*$^{+/-}$ embryos only at 32°C, but not at 18°C (Figure 3G), consistent with Cofilin having potent, heat stress-specific, F-actin-destabilizing activity in embryos. Together, our data support a model whereby heat stress induces an ASR in embryos during which increased Cofilin activity alters the actin cytoskeleton in both the cytoplasm (furrow tip F-actin is destabilized) and the nucleus (actin rods assemble).

F-Actin Destabilization Puts Morphogenesis at Risk in Heat-Stressed Embryos

Although stress responses are typically considered protective, we suspected that F-actin destabilization at furrow tips during embryonic ASR is deleterious and could explain why cellularization shows increased multinucleation at 32°C (Figures 1B and 1C). To examine a causal link between F-actin stability and multinucleation, we genetically modulated F-actin stability using Cofilin and another F-actin binding protein Sry-α. Sry-α is a positive regulator of F-actin levels in furrow tips and was previously shown to promote successful cellularization at 32°C (Zheng et al., 2013). We knocked down Sry-α function in embryos by RNAi (*sry-α*^{RNAi}) and found that F-actin at furrow tips turns over very fast at 32°C, with a half time to recovery of 9.93 ± 1.07 s (mean ± SE; Figure 4A), indicating severe destabilization. Again, no change was seen for the mobile fraction (Figure S4E). F-actin destabilization correlated with frequent multinucleation in *sry-α*^{RNAi} embryos, and *sry-α* null mutants (*sry-α*$^{-/-}$; Figures 4B and 4C). F-actin stability could be restored in *sry-α*^{RNAi} embryos by simultaneously reducing the dosage of Cofilin (*sry-α*^{RNAi} + *cofilin*$^{+/-}$; Figure 4A). This restoration of F-actin stability mitigated the multinucleation phenotype (*sry-α*$^{-/-}$ + *cofilin*$^{+/-}$; Figures 4B and 4C), showing that a minimum level of F-actin stability is required in furrow tips to ensure successful furrow ingression. Thus, the ASR makes cellularization more error-prone by reducing F-actin stability.

Viability, in Addition to Morphogenesis, Is Compromised in Heat-Stressed Embryos

Even if Cofilin-mediated ASR puts cellularization at risk, it could benefit the organism overall (i.e., there might be a trade-off). To address this possibility, we quantified larval hatching rates for wild-type and *cofilin*$^{+/-}$ embryos. Embryos were reared at 18°C or 32°C, collected in late cellularization, and shifted back

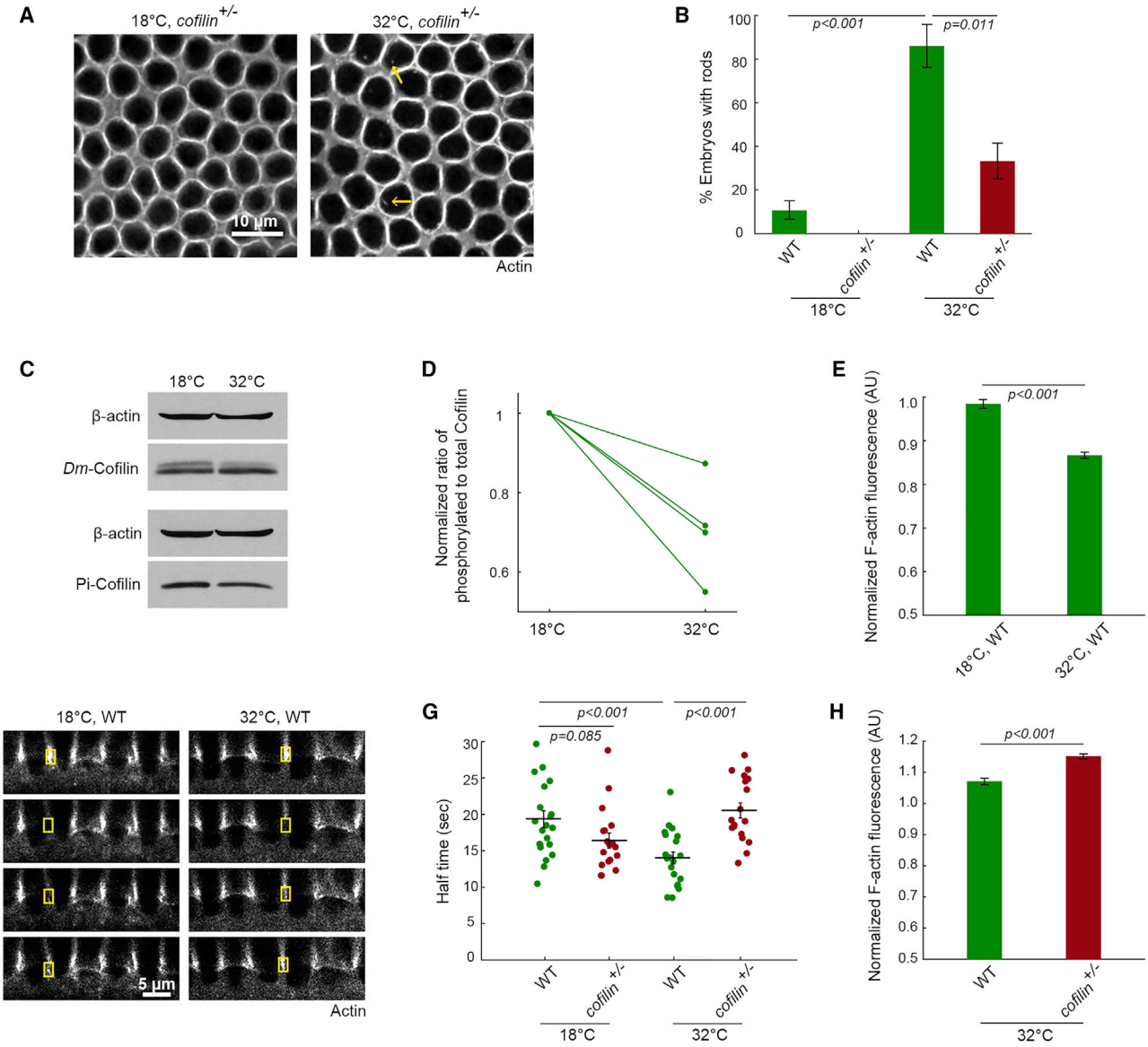

Figure 3. Cofilin Mediates an ASR that Changes Actin Organization in Nuclei and Cytoplasm

(A) Surface views show G-actin^{Red} in furrow tips in *cofilin*$^{+/-}$ embryos at the indicated temperatures. Intra-nuclear rods (yellow arrows) are reduced in *cofilin*$^{+/-}$ embryos at 32°C.

(B) Percentage of embryos with rods in wild-type (WT) and *cofilin*$^{+/-}$ embryos at the indicated temperatures (n ≥ 14 embryos per condition, with ~500 nuclei analyzed per embryo; mean ± SE).

(C) Representative western blots for *Dm*-Cofilin, Pi-cofilin from WT embryos at the indicated temperatures. β-actin is used as a loading control. Antibody validation in Figure S2.

(D) Ratio phosphorylated to total Cofilin in WT embryos at the indicated temperatures (n = 4 independent experiments; mean ± SE).

(E) F-actin levels in furrow tips in WT embryos at the indicated temperatures (n ≥ 29 embryos per temperature, with 15 furrows analyzed per embryo; mean ± SE). Normalization to Histone-GFP embryos at 25°C, according to Figure S3.

(F) Cross sections show FRAP of furrow tip F-actin (G-actin^{Red}) in WT embryos at the indicated temperatures. Yellow boxes show bleached furrow tips. Pre, immediate pre-bleach time point; bleach, immediate post-bleach time point; sec, seconds after bleach.

(G) FRAP kinetics for furrow tip F-actin in WT and *cofilin*$^{+/-}$ embryos at indicated temperatures. Each point represents one embryo (n ≥ 14 embryos per temperature, with 1–3 furrows analyzed per embryo; horizontal lines represent means ± SE).

(H) F-actin levels in furrow tips in WT and *cofilin*$^{+/-}$ embryos at 32°C (n ≥ 48 embryos per condition, with 15 furrows analyzed per embryo; mean ± SE). Normalization to Histone-GFP embryos at 32°C.

(E) and (H) correspond to scatterplots in Figures S4C and S4D.

Student's t test used to calculate p values in (B), (E), (G), and (H).

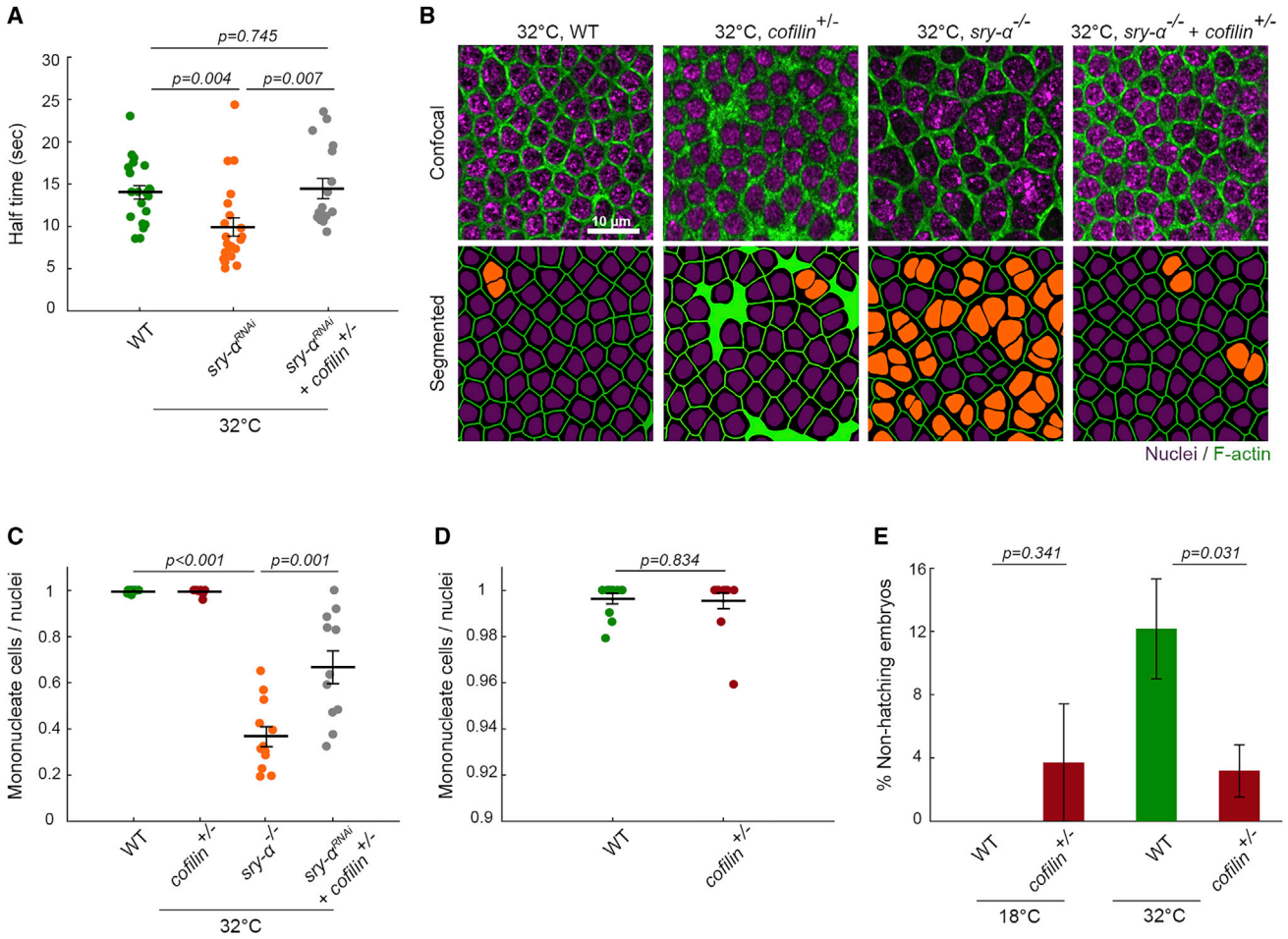

Figure 4. ASR Is Maladaptive for Cellularization and Embryo Development

(A) FRAP kinetics for furrow tip F-actin in embryos of indicated genotypes at 32°C. Each point represents one embryo (n ≥ 14 embryos per genotype, with 1–3 furrows analyzed per embryo).

(B) Surface views show furrow tip F-actin (phalloidin, green) and nuclei (Hoechst, purple) in embryos of indicated genotypes at 32°C. Multinucleate cells highlighted by orange nuclei in corresponding segmented images.

(C) Severity of multinucleation in embryos of indicated genotypes at 32°C. Each point represents one embryo (n ≥ 11 embryos per genotype, with ~150 nuclei analyzed per embryo).

(D) Data from (4C) on shortened y axis to show no difference between wild-type (WT) and *cofilin*$^{+/-}$ embryos.

(E) Larval hatching rates for indicated conditions (n ≥ 5 independent experiments, with ≥ 9 embryos per experiment; mean ± SE). Corresponding scatterplot in Figure S4F.

Student's t test used to calculate p values in (A), (C), (D), and (E).

Horizontal lines represent means ± SE in (A), (C), and (D).

to room temperature until larval hatching was scored (Table S1). For the 32°C embryo group, more *cofilin*$^{+/-}$ embryos survived and hatched than did wild-type (Figures 4E and S4F), suggesting that the ASR is not only disruptive for cellularization but also can be harmful to embryos overall.

We wondered whether the reduced viability of heat-stressed embryos was a result of cellularization mistakes. However, inspection of *cofilin*$^{+/-}$ embryos showed a similar likelihood of furrow regressions as seen in wild-type embryos (Figures 4C and 4D). We do not know why overstabilization of F-actin at 32°C in *cofilin*$^{+/-}$ embryos causes multinucleation, though our combined data suggest that some "precise" level of stability is required for best cellularization outcomes. Nonetheless, *cofilin*$^{+/-}$ embryos had improved viability compared to wild-type embryos, even though they showed the same extent of multinucleation as wild-type. Thus, embryos must be robust to a small number of furrow regressions. Instead, the reduced viability accompanying ASR seems more closely associated with F-actin destabilization in the cytoplasm, perhaps due to more free actin entering the nucleus.

DISCUSSION

Here, we identify an embryonic ASR. While previously ASR was defined in terms of actin rod assembly (e.g., Kanellos and Frame, 2016), our work argues that the actin cytoskeleton is more

extensively modified throughout cells. We suggest a model whereby increased Cofilin activity during ASR in fly embryos leads to increased F-actin severing in the cytoplasm and destabilization of normal F-actin structures. This F-actin destabilization has two consequences: first, it puts morphogenesis at risk. Specifically, during cellularization, F-actin destabilization at all furrow tips leads to the stochastic regression of a small number of furrows. Second, cytoplasmic F-actin destabilization increases the free actin monomer pool in the cytoplasm and, consequently, the nucleus, to a level that can promote concentration-dependent actin rod assembly in the nucleus. Rod assembly buffers free nuclear actin levels, perhaps in an attempt to sequester subunits from some adverse function in either the nucleus or cytoplasm. While many details of this model remain to be tested, we believe that the ASR should now be viewed in terms of the entire actin cytoskeleton and all its functions, both nuclear and cytoplasmic.

This work adds to a growing list of examples in which Cofilin emerges as a specific target for, and vulnerability to, environmental stress. Beyond the ASR, Cofilin oxidation and responsiveness to heat shock proteins in environmentally stressed cells affects actin-based behaviors, as well as cell survival via mitochondrial health and apoptotic signaling (Klamt et al., 2009; Klemke et al., 2008; Simard et al., 2011). While Cofilin's functions will surely differ with context, we suggest it as a key general node in actin-based stress response, acting across diverse cell types and organisms. Our observations in the fly embryo lead us to consider whether stress-induced changes in Cofilin activity could partially explain why high temperature is teratogenic (Auger et al., 2017; Chambers et al., 1998; Dixon et al., 2011; Edwards 2006). Because F-actin remodeling drives morphogenesis (Rodal et al., 2015), we think it possible that Cofilin-mediated stress response could compromise the fidelity of other morphogenetic events, just as it precipitated cellularization failures here. In addition, by changing the levels or organization of nuclear actin, Cofilin-mediated ASR could also alter nuclear events critical to development, including transcription and genome remodeling.

STAR★METHODS

Detailed methods are provided in the online version of this paper and include the following:

- KEY RESOURCES TABLE
- CONTACT FOR REAGENT AND RESOURCE SHARING
- EXPERIMENTAL MODEL AND SUBJECT DETAILS
  - Fly stocks and genetics
- METHOD DETAILS
  - Embryo collection, fixation, and staining
  - Hatching assay
  - Rhodamine G-actin injections and RNAi
  - Image acquisition
  - Western Blotting
  - Antibody production and validation
  - Phosphatase assay
- QUANTIFICATION AND STATISTICAL ANALYSIS
  - Multinucleation quantification
  - F-actin levels quantification
  - FRAP quantification
  - Actin rod abundance quantification
  - Western blot quantification
- DATA AND SOFTWARE AVAILABILITY

SUPPLEMENTAL INFORMATION

Supplemental Information can be found with this article online at https://doi.org/10.1016/j.celrep.2019.02.092.

ACKNOWLEDGMENTS

We gratefully acknowledge the computing resources provided by the CIBR Center of Baylor College of Medicine. This work was supported by grants from the NIH (R01 GM115111 to L.F., L.Z., Z.X., H.S., and A.M.S.; T32 GM008231 to N.B.). S.C. and I.G. are supported by a grant from the NIH (R01 GM082837), grants from the NSF (PHY-1147498, PHY-1430124, and PHY-1427654), a John S. Dunn Collaborative Research Award, and a Welch Foundation grant (Q-1759).

AUTHOR CONTRIBUTIONS

L.Z. and A.M.S. conceived of the idea. L.F. and L.Z. performed genetics and imaging. Z.X. and N.B. generated the *Dm*-Cofilin antibody. N.B. performed the biochemistry. L.F. performed the hatching assays. L.Z., L.F., H.S., S.C., I.G., and A.M.S. performed the image and the data analysis. L.Z., L.F., N.B., and S.C. prepared the figures. L.F. and A.M.S. wrote the manuscript.

DECLARATION OF INTERESTS

The authors declare no competing interests.

Received: October 1, 2018
Revised: January 22, 2019
Accepted: February 21, 2019
Published: March 26, 2019

REFERENCES

Amberg, D., Leadsham, J.E., Kotiadis, V., and Gourlay, C.W. (2012). Cellular ageing and the actin cytoskeleton. Subcell. Biochem. *57*, 331–352.

Andrianantoandro, E., and Pollard, T.D. (2006). Mechanism of actin filament turnover by severing and nucleation at different concentrations of ADF/cofilin. Mol. Cell *24*, 13–23.

Ashworth, S.L., and Molitoris, B.A. (1999). Pathophysiology and functional significance of apical membrane disruption during ischemia. Curr. Opin. Nephrol. Hypertens. *8*, 449–458.

Ashworth, S.L., Southgate, E.L., Sandoval, R.M., Meberg, P.J., Bamburg, J.R., and Molitoris, B.A. (2003). ADF/cofilin mediates actin cytoskeletal alterations in LLC-PK cells during ATP depletion. Am. J. Physiol. Renal Physiol. *284*, F852–F862.

Auger, N., Fraser, W.D., Sauve, R., Bilodeau-Bertrand, M., and Kosatsky, T. (2017). Risk of congenital heart defects after ambient heat exposure early in pregnancy. Environ. Health Perspect. *125*, 8–14.

Baird, N.A., Douglas, P.M., Simic, M.S., Grant, A.R., Moresco, J.J., Wolff, S.C., Yates, J.R., 3rd, Manning, G., and Dillin, A. (2014). HSF-1-mediated cytoskeletal integrity determines thermotolerance and life span. Science *346*, 360–363.

Bamburg, J.R., and Bernstein, B.W. (2016). Actin dynamics and cofilin-actin rods in alzheimer disease. Cytoskeleton (Hoboken) *73*, 477–497.

Bamburg, J.R., Bernstein, B.W., Davis, R.C., Flynn, K.C., Goldsbury, C., Jensen, J.R., Maloney, M.T., Marsden, I.T., Minamide, L.S., Pak, C.W., et al. (2010). ADF/cofilin-actin rods in neurodegenerative diseases. Curr. Alzheimer Res. *7*, 241–250.

Bergh, S., and Arking, R. (1984). Development profile of the heat shock response in early embryos of Drosophila. J. Exp. Zool. *231*, 379–391.

Bernstein, B.W., Chen, H., Boyle, J.A., and Bamburg, J.R. (2006). Formation of actin-ADF/cofilin rods transiently retards decline of mitochondrial potential and ATP in stressed neurons. Am. J. Physiol. Cell Physiol. *291*, C828–C839.

Bownes, M. (1975). A photographic study of development in the living embryo of *Drosophila melanogaster*. J. Embryol. Exp. Morphol. *33*, 789–801.

Bravo-Cordero, J.J., Magalhaes, M.A.O., Eddy, R.J., Hodgson, L., and Condeelis, J. (2013). Functions of cofilin in cell locomotion and invasion. Nat. Rev. Mol. Cell Biol. *14*, 405–415.

Cao, J., Albertson, R., Riggs, B., Field, C.M., and Sullivan, W. (2008). Nuf, a Rab11 effector, maintains cytokinetic furrow integrity by promoting local actin polymerization. J. Cell Biol. *182*, 301–313.

Chambers, C.D., Johnson, K.A., Dick, L.M., Felix, R.J., and Jones, K.L. (1998). Maternal fever and birth outcome: a prospective study. Teratology *58*, 251–257.

Chambers, J.E., Dalton, L.E., Clarke, H.J., Malzer, E., Dominicus, C.S., Patel, V., Moorhead, G., Ron, D., and Marciniak, S.J. (2015). Actin dynamics tune the integrated stress response by regulating eukaryotic initiation factor 2α dephosphorylation. eLife *4*, e04872.

Crews, S.M., McCleery, W.T., and Hutson, M.S. (2016). Pathway to a phenocopy: heat stress effects in early embryogenesis. Dev. Dyn. *245*, 402–413.

Dixon, M.J., Marazita, M.L., Beaty, T.H., and Murray, J.C. (2011). Cleft lip and palate: understanding genetic and environmental influences. Nat. Rev. Genet. *12*, 167–178.

Dopie, J., Skarp, K.P., Rajakylä, E.K., Tanhuanpää, K., and Vartiainen, M.K. (2012). Active maintenance of nuclear actin by importin 9 supports transcription. Proc. Natl. Acad. Sci. USA *109*, E544–E552.

Dopie, J., Rajakylä, E.K., Joensuu, M.S., Huet, G., Ferrantelli, E., Xie, T., Jäälinoja, H., Jokitalo, E., and Vartiainen, M.K. (2015). Genome-wide RNAi screen for nuclear actin reveals a network of cofilin regulators. J. Cell Sci. *128*, 2388–2400.

Edwards, M.J. (2006). Review: hyperthermia and fever during pregnancy. Birth Defects Res. A Clin. Mol. Teratol. *76*, 507–516.

Figard, L., and Sokac, A.M. (2011). Imaging cell shape change in living Drosophila embryos. J. Vis. Exp. *49*, 2503.

Figard, L., Xu, H., Garcia, H.G., Golding, I., and Sokac, A.M. (2013). The plasma membrane flattens out to fuel cell-surface growth during Drosophila cellularization. Dev. Cell *27*, 648–655.

Grosshans, J., Wenzl, C., Herz, H.M., Bartoszewski, S., Schnorrer, F., Vogt, N., Schwarz, H., and Müller, H.A. (2005). RhoGEF2 and the formin Dia control the formation of the furrow canal by directed actin assembly during Drosophila cellularisation. Development *132*, 1009–1020.

Hamdoun, A., and Epel, D. (2007). Embryo stability and vulnerability in an always changing world. Proc. Natl. Acad. Sci. USA *104*, 1745–1750.

Hardy, L.R. (2012). Fluorescence recovery after photobleaching (FRAP) with a focus on F-actin. Curr. Protoc. Neurosci. *Chapter 2*, Unit 2.17. https://doi.org/10.1002/0471142301.ns0217s61.

Harlow, E., and Lane, D. (1988). Antibodies: A Laboratory Manual (Cold Spring Harbor Laboratory Press).

Higuchi, R., Vevea, J.D., Swayne, T.C., Chojnowski, R., Hill, V., Boldogh, I.R., and Pon, L.A. (2013). Actin dynamics affect mitochondrial quality control and aging in budding yeast. Curr. Biol. *23*, 2417–2422.

Huang, T.Y., Minamide, L.S., Bamburg, J.R., and Bokoch, G.M. (2008). Chronophin mediates an ATP-sensing mechanism for cofilin dephosphorylation and neuronal cofilin-actin rod formation. Dev. Cell *15*, 691–703.

Iida, K., Iida, H., and Yahara, I. (1986). Heat shock induction of intranuclear actin rods in cultured mammalian cells. Exp. Cell Res. *165*, 207–215.

Kanellos, G., and Frame, M.C. (2016). Cellular functions of the ADF/cofilin family at a glance. J. Cell Sci. *129*, 3211–3218.

Kim, J.S., Huang, T.Y., and Bokoch, G.M. (2009). Reactive oxygen species regulate a slingshot-cofilin activation pathway. Mol. Biol. Cell *20*, 2650–2660.

Klamt, F., Zdanov, S., Levine, R.L., Pariser, A., Zhang, Y., Zhang, B., Yu, L.R., Veenstra, T.D., and Shacter, E. (2009). Oxidant-induced apoptosis is mediated by oxidation of the actin-regulatory protein cofilin. Nat. Cell Biol. *11*, 1241–1246.

Klemke, M., Wabnitz, G.H., Funke, F., Funk, B., Kirchgessner, H., and Samstag, Y. (2008). Oxidation of cofilin mediates T cell hyporesponsiveness under oxidative stress conditions. Immunity *29*, 404–413.

McCullough, B.R., Blanchoin, L., Martiel, J.L., and De la Cruz, E.M. (2008). Cofilin increases the bending flexibility of actin filaments: implications for severing and cell mechanics. J. Mol. Biol. *381*, 550–558.

Merrill, P.T., Sweeton, D., and Wieschaus, E. (1988). Requirements for autosomal gene activity during precellular stages of Drosophila melanogaster. Development *104*, 495–509.

Minamide, L.S., Striegl, A.M., Boyle, J.A., Meberg, P.J., and Bamburg, J.R. (2000). Neurodegenerative stimuli induce persistent ADF/cofilin-actin rods that disrupt distal neurite function. Nat. Cell Biol. *2*, 628–636.

Minamide, L.S., Maiti, S., Boyle, J.A., Davis, R.C., Coppinger, J.A., Bao, Y., Huang, T.Y., Yates, J., Bokoch, G.M., and Bamburg, J.R. (2010). Isolation and characterization of cytoplasmic cofilin-actin rods. J. Biol. Chem. *285*, 5450–5460.

Mukhina, S., Wang, Y.L., and Murata-Hori, M. (2007). Alpha-actinin is required for tightly regulated remodeling of the actin cortical network during cytokinesis. Dev. Cell *13*, 554–565.

Munsie, L.N., and Truant, R. (2012). The role of the cofilin-actin rod stress response in neurodegenerative diseases uncovers potential new drug targets. Bioarchitecture *2*, 204–208.

Munsie, L.N., Desmond, C.R., and Truant, R. (2012). Cofilin nuclear-cytoplasmic shuttling affects cofilin-actin rod formation during stress. J. Cell Sci. *125*, 3977–3988.

Ohta, Y., Nishida, E., Sakai, H., and Miyamoto, E. (1989). Dephosphorylation of cofilin accompanies heat shock-induced nuclear accumulation of cofilin. J. Biol. Chem. *264*, 16143–16148.

Ono, S., Abe, H., Nagaoka, R., and Obinata, T. (1993). Colocalization of ADF and cofilin in intranuclear actin rods of cultured muscle cells. J. Muscle Res. Cell Motil. *14*, 195–204.

Padash Barmchi, M., Rogers, S., and Häcker, U. (2005). DRhoGEF2 regulates actin organization and contractility in the Drosophila blastoderm embryo. J. Cell Biol. *168*, 575–585.

Parman, T., Wiley, M.J., and Wells, P.G. (1999). Free radical-mediated oxidative DNA damage in the mechanism of thalidomide teratogenicity. Nat. Med. *5*, 582–585.

Phair, R.D., Gorski, S.A., and Misteli, T. (2004). Measurement of dynamic protein binding to chromatin in vivo, using photobleaching microscopy. Methods Enzymol. *375*, 393–414.

Puscheck, E.E., Awonuga, A.O., Yang, Y., Jiang, Z., and Rappolee, D.A. (2015). Molecular biology of the stress response in the early embryo and its stem cells. Adv. Exp. Med. Biol. *843*, 77–128.

Rodal, A.A., Del Signore, S.J., and Martin, A.C. (2015). *Drosophila* comes of age as a model system for understanding the function of cytoskeletal proteins in cells, tissues, and organisms. Cytoskeleton (Hoboken) *72*, 207–224.

Salilew-Wondim, D., Tesfaye, D., Hoelker, M., and Schellander, K. (2014). Embryo transcriptome response to environmental factors: implication for its survival under suboptimal conditions. Anim. Reprod. Sci. *149*, 30–38.

Sanger, J.W., Gwinn, J., and Sanger, J.M. (1980). Dissolution of cytoplasmic actin bundles and the induction of nuclear actin bundles by dimethyl sulfoxide. J. Exp. Zool. *213*, 227–230.

Schindelin, J., Arganda-Carreras, I., Frise, E., Kaynig, V., Longair, M., Pietzsch, T., Preibisch, S., Rueden, C., Saalfeld, S., Schmid, B., et al. (2012). Fiji: an open-source platform for biological-image analysis. Nat. Methods *9*, 676–682.

Schwartz, N., Hosford, M., Sandoval, R.M., Wagner, M.C., Atkinson, S.J., Bamburg, J., and Molitoris, B.A. (1999). Ischemia activates actin

depolymerizing factor: role in proximal tubule microvillar actin alterations. Am. J. Physiol. *276*, F544–F551.

Simard, J.P., Reynolds, D.N., Kraguljac, A.P., Smith, G.S., and Mosser, D.D. (2011). Overexpression of HSP70 inhibits cofilin phosphorylation and promotes lymphocyte migration in heat-stressed cells. J. Cell Sci. *124*, 2367–2374.

Sokac, A.M., and Wieschaus, E. (2008). Zygotically controlled F-actin establishes cortical compartments to stabilize furrows during Drosophila cellularization. J. Cell Sci. *121*, 1815–1824.

Vandebrouck, A., Domazetovska, A., Mokbel, N., Cooper, S.T., Ilkovski, B., and North, K.N. (2010). In vitro analysis of rod composition and actin dynamics in inherited myopathies. J. Neuropathol. Exp. Neurol. *69*, 429–441.

Xue, Z., and Sokac, A.M. (2016). -Back-to-back mechanisms drive actomyosin ring closure during Drosophila embryo cleavage. J. Cell Biol. *215*, 335–344.

Zheng, L., Sepúlveda, L.A., Lua, R.C., Lichtarge, O., Golding, I., and Sokac, A.M. (2013). The maternal-to-zygotic transition targets actin to promote robustness during morphogenesis. PLoS Genet. *9*, e1003901.

STAR★METHODS

KEY RESOURCES TABLE

REAGENT or RESOURCE	SOURCE	IDENTIFIER
Antibodies		
Anti-β-actin, mouse	SCBT	Cat#sc-47778; RRID: AB_626632
Anti-*Drosophila melanogaster* Cofilin (*Dm*-Cofilin), rabbit	This study	N/A
Anti-PhosphoCofilin (P_i-Cofilin), rabbit	SCBT	Cat#sc-12912-R; RRID:AB_673572
Anti-Mouse HRP	Jackson Immuno Research	Cat#115-035-003; RRID:AB_10015289
Anti-Rabbit HRP	Jackson Immuno Research	Cat#111-035-144; RRID:AB_2307391
Bacterial and Virus Strains		
BL21 (DE3)	Thermo Scientific	Cat#C600003
Chemicals, Peptides, and Recombinant Proteins		
Actin protein (rhodamine), human platelet (G-actin^{red})	Cytoskeleton, Inc.	Cat#APHL99-E
6X-His-*Dm*-Cofilin	This study	N/A
Alexa Fluor 488 phalloidin	Invitrogen/Thermo Scientific	Cat#A12379
Alexa Fluor 546 phalloidin	Invitrogen/Thermo Scientific	Cat#A22283
Hoechst 33342	Invitrogen/Fisher Scientific	Cat#H3570
Halocarbon 27 oil	Sigma-Aldrich	Cat#H8773-100ML
Halocarbon 700 oil	Sigma-Aldrich	Cat#H8898-100ML
Nickel-NTA Agarose	QIAGEN	Cat#30210
Pierce Protease Inhibitor Mini Tablets, EDTA-free	Thermo Scientific	Cat#A32955
Critical Commercial Assays		
Melon Gel IgG Spin Purification Kit	Thermo Scientific	Cat#45206
Lambda phosphatase	SCBT	Cat#sc-200312A
BCA Protein Assay	Thermo Scientific	Cat#23225
Pierce Disposable Columns (10 mL)	Thermo Scientific	Cat#29924
Amicon-Ultra 15 mL centrifugal filters, MWCO 30 kDa	Millipore-Sigma	Cat#UFC903008
Experimental Models: Organisms/Strains		
Oregon R (OreR)	DGGR	Cat#109612; RRID:DGGR_109612
ubi::H2A-GFP (Histone-GFP)	Gift of E. Wieschaus	N/A
tsr^1/CyO (1/2 cofilin)	BDSC	Cat#9107; RRID:BDSC_9107
Df(3R)X3F/TM3, Sb (sry-α −/−)	Merrill et al., 1988	N/A
Oligonucleotides		
Primer: Forward: *sry-α*-RNAi-F (5′-TAATACGACTCACTATAGGGTCAGGAGCTAATC-3′); Reverse: *sry-α*-RNAi-R (5′-TAATCAGACTCACTATAGGGCCCAGCATGTCCA-3′)	Zheng et al., 2013	N/A
Recombinant DNA		
pET45b-tsr(B/X) (6X-His-*Dm*-Cofilin)	This study	N/A
Software and Algorithms		
ImageJ/FIJI	NIH	https://fiji.sc
Adobe Photoshop CC	Adobe	https://www.adobe.com/creativecloud.html
Adobe Illustrator CC	Adobe	https://www.adobe.com/creativecloud.html
MATLAB	MathWorks	https://www.mathworks.com/products/matlab.html
Segmentation Algorithm (custom MATLAB code)	Zheng et al., 2013	N/A
Furrow tracking algorithm (custom MATLAB code)	Zheng et al., 2013	N/A
Furrow canal intensity algorithm (custom MATLAB code)	Zheng et al., 2013	N/A

CONTACT FOR REAGENT AND RESOURCE SHARING

Further information and requests for resources and reagents should be directed to the Lead Contact, Anna Marie Sokac (sokac@bcm.edu).

EXPERIMENTAL MODEL AND SUBJECT DETAILS

Drosophila melanogaster stocks were housed at 22°C on standard molasses food. Most analyses focus on embryos in Bownes Stages 4 through 5 (pre-cellularization through the end of cellularization) (Bownes, 1975), unless noted in the Method Details, such as mixed-stage embryo collections for some Western Blotting experiments.

Fly stocks and genetics

OreR was used as the wild-type stock. For Histone-GFP, embryos were collected from *ubi::H2A-GFP* (gift of E. Wieschaus). For *cofilin*$^{+/-}$, adults from stock *tsr*^{1}*/CyO* (Bloomington Stock Center #9107) were crossed with OreR, and F2 embryos collected from F1 *tsr*^{1}/+ females crossed with either sibling *tsr*^{1}/+ males (imaging and western blotting experiments) or OreR males (larval hatching assays). For *sry-*$\alpha^{-/-}$, embryos were collected from *Df(3R)X3F/TM3, Sb* (Merrill et al., 1988). For *sry-*$\alpha^{-/-}$ + *cofilin*$^{+/-}$, adults from stock *tsr*^{1}*/CyO* were crossed with *Df(3R)X3F/TM3, Sb*, and F2 embryos collected from F1 *tsr*^{1}/+*; Df(3R)X3F*/+ females crossed with sibling *tsr*^{1}/+*; Df(3R)X3F*/+ males.

METHOD DETAILS

Embryo collection, fixation, and staining

Embryo collection cups were set up on apple juice plates at 18°C or 32°C according to published protocols (Figard and Sokac, 2011). For F-actin staining, mixed-stage embryos were fixed in 8% paraformaldehyde in 0.1 M phosphate buffer (pH 7.4): n-heptane (1:1) and hand-peeled for staining with 5 U ml^{-1} Alexa Fluor 488 phalloidin or Alexa Fluor 546 phalloidin (Thermo Scientific, Rockford, IL). For nuclear staining, Hoescht 33342 was used at 1.0 μg ml^{-1} (Invitrogen, Carlsbad, CA).

Hatching assay

Embryos were reared in collection cups at 18°C or 32°C, following the scheme shown in Table S1. Late cellularization-stage embryos were hand-selected under a dissecting microscope, transferred to fresh apple juice plates, covered in Halocarbon oil 27 (Sigma Aldrich, St. Louis, MO), and incubated at 22°C in humidifying chambers (80x15 mm glass Petri dish lined with moist paper towels). After 48 hours plates were scored for the percent of hatched larvae.

Rhodamine G-actin injections and RNAi

Embryos were collected 30 minutes post-egg laying from collection cups at 18°C. Embryos were mounted in a line on the edge of a glass coverslip with "embryo glue" (a solution made from double-sided tape saturated in n-heptane), dessicated for 7-10 minutes prior to injection, and covered with 1:3 mixture of Halocarbon 700:Halocarbon 27. Lyophilized, rhodamine-labeled, non-muscle G-actin (G-actin^{Red}; Cytoskeleton, Inc., Denver, CO) was resuspended at 5 μg/μl with 1 μL water and 1 μL G-buffer (5 mM Tris-HCl pH 8.0, 0.2 mM ATP, 0.5 mM DTT, and 0.2 mM $CaCl_2$), and ~1 μL of the solution was loaded into a glass capillary needle. Using a custom injection stage and Femtojet Express microinjector (Eppendorf, Hamburg, Germany), ~50 pl of the solution was injected per embryo. Following injection, embryos were incubated at 18°C or 32°C until imaging (Table S1). For *sry-*α^{RNAi}, embryos were prepared as follows: G-actin^{Red} was resuspended at 5 μg/μl in *sry-*α double-stranded RNA, previously diluted 1:1 with G-buffer, and ~50 pl was injected per embryo. Double-stranded RNAs for *sry-*α were prepared as previously described, using primers: *sry-*α-RNAi-F (5′-TAATACGACTCACTATAGGGTCAGGAGCTAATC-3′) and *sry-*α-RNAi-R (5′-TAATCAGACTCACTATAGGGCC CAGCATGTCCA-3′) (Zheng et al., 2013). To confirm that neither G-actin^{Red} injection nor FRAP perturbed cellularization, furrow ingression rates were estimated using a custom MATLAB furrow tracking algorithm in wild-type embryos following these manipulations, and were found to be comparable to published rates of furrow ingression for wild-type embryos (Figard et al., 2013).

Image acquisition

Images were collected on a Zeiss LSM 710 confocal microscope with a 40X/1.2 numerical aperture water-immersion objective (Carl Zeiss, Inc., Oberkochen, Germany). For presentation, images were cropped, resized, and adjusted for brightness and contrast in ImageJ/FIJI (Schindelin et al., 2012) or Adobe Photoshop CC (Adobe, San Jose, CA). Channels were adjusted separately in multicolor images.

For FRAP, embryos were imaged at 18 ± 2°C or at 32 ± 2°C in a thermal incubator. G-actin^{Red} was bleached to approximately 50% fluorescence intensity using 100% laser power in cross-section within a 2 μm x 1 μm box for furrow canals or in surface views within a 2 μm x 2 μm box for rods. Fluorescence recovery was recorded at 1 or 2 s intervals for ≥ 80 s, which encompassed the time to full recovery. Bleached furrow canals ingress at the same rate and with the same morphology as their unbleached neighbors, suggesting that bleaching does not induce significant phototoxicity (Figure 3F; Xue and Sokac, 2016).

For imaging actin rods, wild-type or Histone-GFP embryos injected with G-Actin^{Red} were imaged at 18 ± 2°C or at 32 ± 2°C in a thermal incubator, ~10 μm beneath the embryo's surface, at the mid-section of the nuclei.

Western Blotting

Embryos (200 per condition) in early cellularization were hand-selected under a dissecting microscope and rapidly snap-frozen in liquid nitrogen. Frozen embryos were homogenized on ice in lysis buffer (150 μL 0.05 M Tris pH 8.0, 0.15 M KCl, 0.05M EDTA, 0.5% NP-40, 1X protease inhibitor cocktail (Pierce Protease Inhibitor Mini Tablets, EDTA-free, Thermo Scientific)). After spinning to remove yolk and debris, protein concentrations were determined using a BCA Protein Assay (Thermo Scientific). Equal amounts of protein were loaded per well and separated on hand-cast 12% SDS-PAGE gels. Proteins were transferred to 0.2 μm nitrocellulose (Bio-Rad, Hercules, CA) and probed with 1:50 mouse anti-β-actin (sc-47778, Santa Cruz Biotechnology, Dallas, TX), 1:5000 rabbit anti-*Dm*-Cofilin, or 1:5000 rabbit anti-P_i-Cofilin (sc-12912-R, Santa Cruz Biotechnology), followed by 1:5000 goat anti-mouse HRP or 1:10,000 goat anti-rabbit HRP secondary antibodies (Jackson Immuno Research, West Grove, PA).

Antibody production and validation

Recombinant protein 6X-His-*Dm*-Cofilin (Twinstar) was expressed in *E. coli* strain BL21 and purified in gravity-flow columns (Thermo Scientific) using Nickel-NTA affinity beads (QIAGEN, Hilden, Germany). Antibody was raised in rabbits by Covance (Princeton, NJ), and precipitated from sera using ammonium sulfate (Harlow and Lane, 1988). IgG was further purified using the Melon Gel Purification Kit (Thermo Scientific).

Phosphatase assay

Collections of mixed-stage embryos were snap-frozen in microcentrifuge tubes in liquid nitrogen. Frozen embryos were homogenized on ice in EDTA-free lysis buffer (200 μL 0.05 M Tris pH 8.0, 0.15 M KCl, 0.5% NP-40, 1X protease inhibitor cocktail (Pierce Protease Inhibitor Mini Tablets, EDTA-free, Thermo Scientific)). For lysates with phosphatase inhibitor, final concentration of 0.04 M sodium orthovanadate (Santa Cruz Biotechnology) and 0.20 M sodium fluoride (Sigma Aldrich) were included in the lysis buffer. For phosphatase reactions, 80 μg embryo protein (calculated from BCA assay, Thermo Scientific) were incubated with 4000 units of λ phosphatase in λ phosphatase reaction buffer supplemented with $MnCl_2$ per the manufacturer's instructions (Santa Cruz Biotechnology) for 20 minutes at 30°C. Equal concentrations of protein from each reaction were separated on hand-cast 12% SDS-PAGE gels, followed by Western Blotting.

QUANTIFICATION AND STATISTICAL ANALYSIS

Student's t tests were performed using GraphPad QuickCalcs (GraphPad, San Diego, CA). Comparisons with p values $\leq$ 0.05 were considered to be significant. Specific information regarding p values and n values can be found in the figure legends. All graphs were generated in MATLAB (MathWorks, Natick, MA) and edited in Adobe Illustrator CC (Adobe, San Jose, CA). Figures were assembled in Adobe Photoshop CC.

Multinucleation quantification

The percent of embryos displaying multinucleation was counted manually using raw, single plane, surface view images collected at the furrow canals, where an entire embryo side was visible ($\geq$1000 nuclei assayed per embryo). The ratio of mononucleate cells to nuclei was determined by manually counting in two quadrants from a raw, single plane, surface view image collected at the furrow canals (quadrant size = 2500 μm^2); and the mean was calculated per embryo. For presentation of the multinucleation phenotype, images were segmented using our previously described custom MATLAB code (Zheng et al., 2013).

F-actin levels quantification

We quantified F-actin levels in furrow tips of embryos with 3-6 μm furrow lengths using custom MATLAB code, as previously described (Zheng et al., 2013), with the following modification: To control for tube-to-tube variation in immunostaining, we used Histone-GFP embryos collected at 25°C (for temperature comparisons) or 32°C (for genotype comparisons) as internal controls that were mixed into each tube of experimental wild-type or *cofilin*$^{+/-}$ embryos collected at either 18°C or 32°C, following the scheme shown in Table S1. GFP signal distinguished the experimental embryos from Histone-GFP controls. We confirmed that differences between wild-type and Histone-GFP embryos at 25°C were insignificant, with a ratio of 1.006 ± 0.035 (n = 3 experiments from 37 embryos for each genotype; mean ± SE). Thus, we normalized F-actin levels as follows: The F-actin fluorescence value from each embryo in an experimental group was normalized to the F-actin fluorescence value from each Histone-GFP embryo in the same tube, generating a pairwise series of normalized F-actin levels. To compare between experimental conditions, pairwise normalized F-actin levels were pooled from each experimental condition (temperature or genotype) and used to calculate average and standard error of the mean. An alternative method, in which F-actin levels from each embryo in an experimental group were normalized to the average of the corresponding Histone-GFP embryos, was also performed and gave similar results.

FRAP quantification

Fluorescence intensity was measured using FIJI/ImageJ. Intensity of the bleached furrow canal (I_{FRAP}) was normalized (I_{NORM}) by the intensity of an unbleached furrow canal (I_{REF}) and the data fitted using two methods (Hardy, 2012; Phair et al., 2004). In both methods, $I_{REF\text{-}PRE}$ and $I_{FRAP\text{-}PRE}$ are the pre-bleach fluorescence intensity in the respective region, and I_0 is the normalized intensity after bleach. In method 1: $I_{NORM}(t) = (I_{FRAP}(t)*I_{REF\text{-}PRE})/(I_{FRAP\text{-}PRE}*I_{REF}(t))$. Using MATLAB, recovery was fit to a single exponential function: $I_{NORM}(t) = I_{max}\text{-}(I_{max}\text{-}I_0)*e^{(-k*t)}$. In method 2: $I_{NORM}(t) = I_{FRAP}(t)/I_{FRAP\text{-}PRE}$. Using MATLAB, recovery was fit to a modified exponential function: $I_{NORM}(t) = I_{max}\text{-}(I_{max}\text{-}I_0)*e^{(-k*t)}\text{-}K_a*t$, where K_a is the acquisition bleaching rate calculated by the slope of the reference fluorescence intensity. For both methods, the mobile fraction and half-time to recovery were calculated by the following equations: Mobile fraction = $(I_{max}\text{-}I_0)\text{-}(1\text{-}I_0)$ and Half time = $-\ln(0.5)/k$. The mobile fraction and half-time values calculated using method 1 are plotted throughout. The same trends were confirmed using method 2.

Actin rod abundance quantification

For rod quantifications, we chose G-actin^{Red} imaging in live embryos to avoid confounding results that were likely to be introduced by poor retention of rods in chemically fixed embryos. (Note that while rods could be minimally preserved by fixation and stained with phalloidin in some embryos, to the eye, rod numbers and size were drastically reduced compared to live embryos). To compare rod formation between temperatures and genotypes, we quantified the percent embryos containing rods within each experiment. However, the same trends were confirmed using two additional measurements of rod abundance: rods per nucleus, as well as percent nuclei containing rods.

For rod abundance quantifications, the total number of nuclei and rods were manually counted and expressed as a ratio (rods / nucleus). Each image was assigned a code so that the experimenter performing the quantifications was blind to the conditions. Free nuclear actin fluorescence and free cytoplasmic actin fluorescence were quantified by averaging fluorescence measurements from 2 μm x 2 μm boxes in three nuclei or three cytoplasmic (non-furrow) regions per embryo. To generate the plots in Figure 2C, 2D, S1E, S1F, and S1G, MATLAB was used to bin data along the x axis with equal numbers of data points in each bin. Binned data were fit to a Hill Function.

Western blot quantification

Films were scanned in black and white at 600 dpi and quantified after applying the ''Subtract Background'' algorithm in Fiji/ImageJ and then inverting. Per blot (bit depth = 8), integrated intensities for each band were normalized against the value of the 18°C band for that antibody or Cofilin species (i.e., phosphorylated or de-phosphorylated) so that results from different experiments could be related. The average and standard deviation for the normalized values for eight or four experiments for actin or Cofilin, respectively, were calculated. *Dm*-Cofilin blots were used to calculate the ratio of phosphorylated to total Cofilin. Consistent with the decrease in this ratio, the P_i-Cofilin values consistently decreased in four out of four experiments.

DATA AND SOFTWARE AVAILABILITY

All raw data, image files, and custom MATLAB algorithms are available upon request to the Lead Contact.

Cell Reports, Volume *26*

Supplemental Information

Cofilin-Mediated Actin Stress Response Is Maladaptive in Heat-Stressed Embryos

Lauren Figard, Liuliu Zheng, Natalie Biel, Zenghui Xue, Hasan Seede, Seth Coleman, Ido Golding, and Anna Marie Sokac

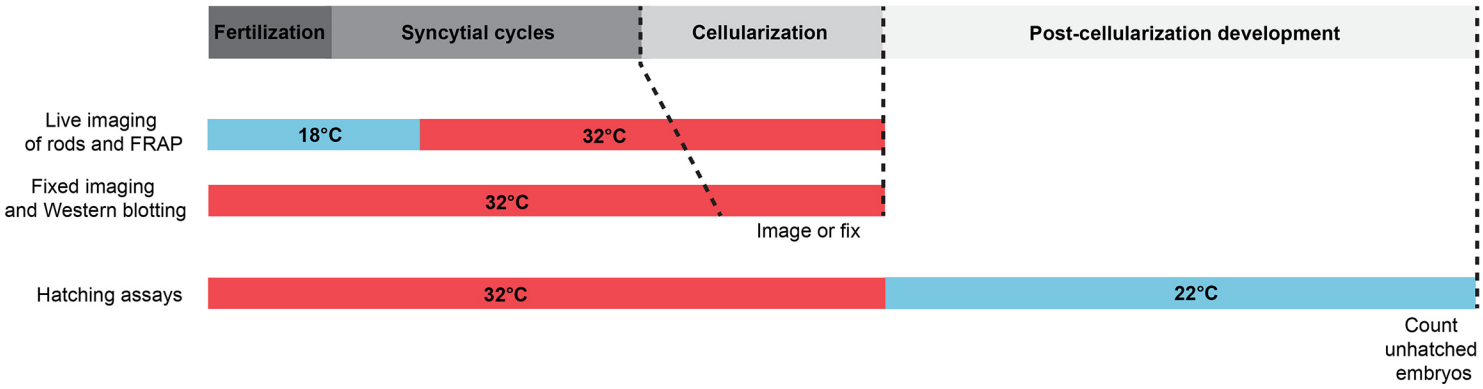

Table S1. Timeline of heat stress experiments. Related to Figures 1-4.
Schematic representation of the developmental timing of heat stress treatments for various experiments.

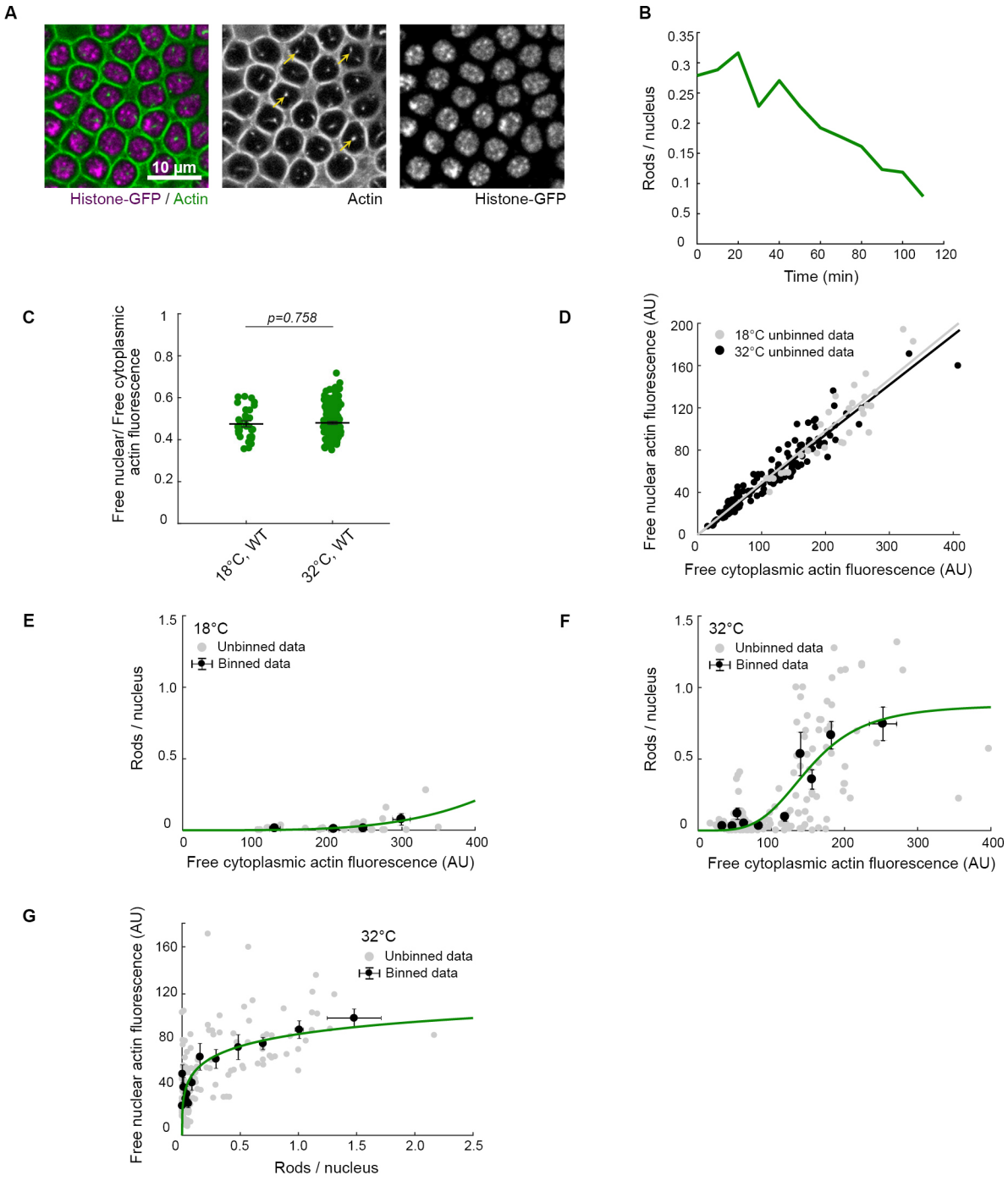

Figure S1. Intra-nuclear actin rods assemble in heat stressed embryos. Related to Figure 2.
(A) Surface views show G-actin^{Red} (green) in furrow tips encircling nuclei (Histone-GFP, purple) in live wild-type (WT) embryos at 32°C. Rods (yellow arrows) assemble inside nuclei. (B) Rod abundance (rods / nucleus) in a single live embryo after downshift from heat stress at 32°C. (C) Ratio of free nuclear to free cytoplasmic actin fluorescence at indicated temperatures (n=147 embryos, with free actin fluorescence averaged from 3 nuclear or cytoplasmic regions per embryo). Each point represents one embryo. Horizontal lines are means ± SE. (D) Free nuclear versus free cytoplasmic actin fluorescence in live WT embryos at indicated temperatures (n=147 embryos, with free actin fluorescence intensity averaged from 3 nuclear or cytoplasmic regions per embryo). Each gray or black point represents one embryo at 18°C or 32°C, respectively. Gray or black lines are linear fits for corresponding data at 18°C or 32°, and fits yield slopes that are statistically indistinguishable. (E) and (F) Rod abundance (rods / nucleus) versus free cytoplasmic actin fluorescence in live WT embryos at indicated temperatures (n≥31 embryos, with rod abundance counted in ≥60 nuclei per embryo; free actin fluorescence averaged from 3 cytoplasmic regions per embryo). Related data shown in Figure 2C, 2D. (G) Free nuclear actin fluorescence versus rod abundance (rods / nucleus) in live WT embryos at 32°C (n=147 embryos, with rod abundance counted in ≥60 nuclei per embryo; free actin fluorescence averaged from 3 nuclei per embryo). Related data shown in Figure 2D.
Each gray point represents one embryo, and black points are binned data (mean ± SE) in (E), (F), and (G).
Green line is binned data fitted to a Hill Function with Hill Coefficient=4 in (E) and (F), and Hill Coefficient=3.5 in (G).
Student's t-test used to calculate P value in (C).

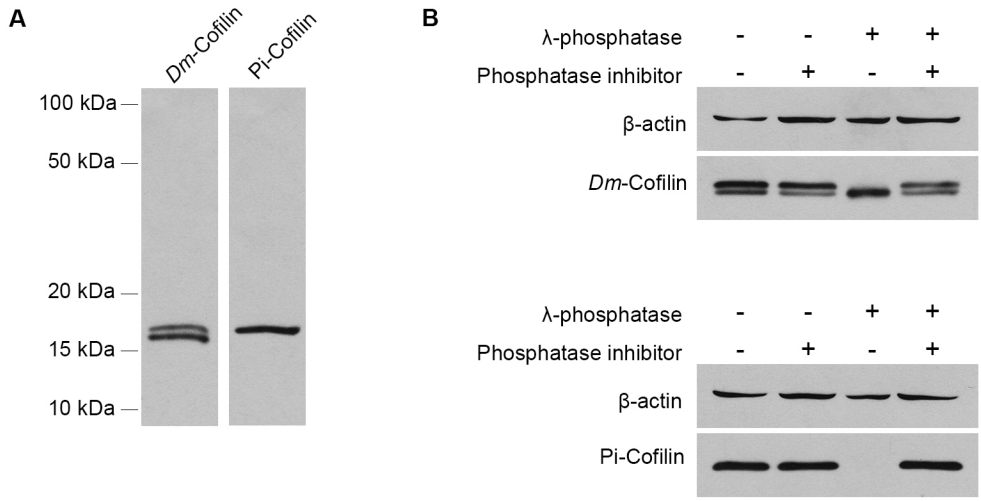

Figure S2. Validation of Dm-Cofilin and Pi-Cofilin antibodies. Related to Figure 3.
(A) Representative full lane Western blots for Dm-Cofilin and Pi-Cofilin antibodies from wild-type embryos at 25°C.
(B) Representative Western blots for Dm-Cofilin and Pi-Cofilin antibodies for lysates from wild-type embryos following indicated λ-phosphatase or Phosphatase inhibitor treatments. β-actin used as loading control.

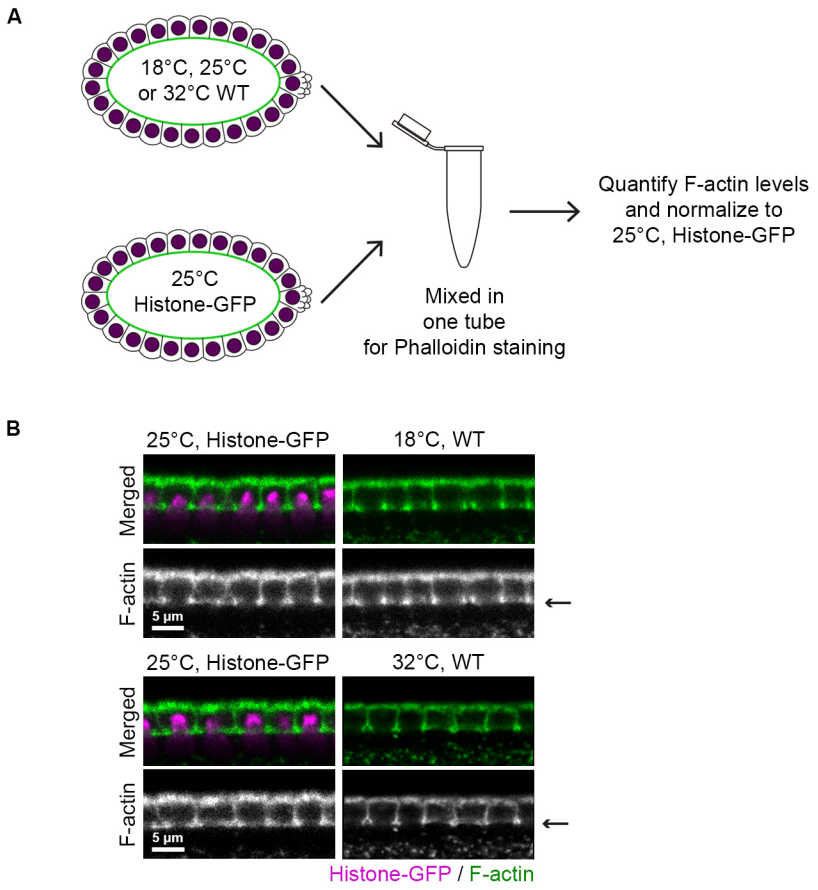

Figure S3. Method used to quantify F-actin levels in embryos reared at different temperatures. Related to Figure 3.
(A) Strategy used to quantify F-actin levels in embryos reared at different temperatures. To minimize experimental variability, embryos reared at each temperature were stained in the same tube as and normalized against internal control, Histone-GFP embryos reared at 25°C. (B) Cross sections show furrow tip F-actin (Phalloidin, green) and nuclei (Histone-GFP purple) in Histone-GFP and wild-type (WT) embryos at indicated temperatures. Arrows indicate furrow tip position where quantification was done.

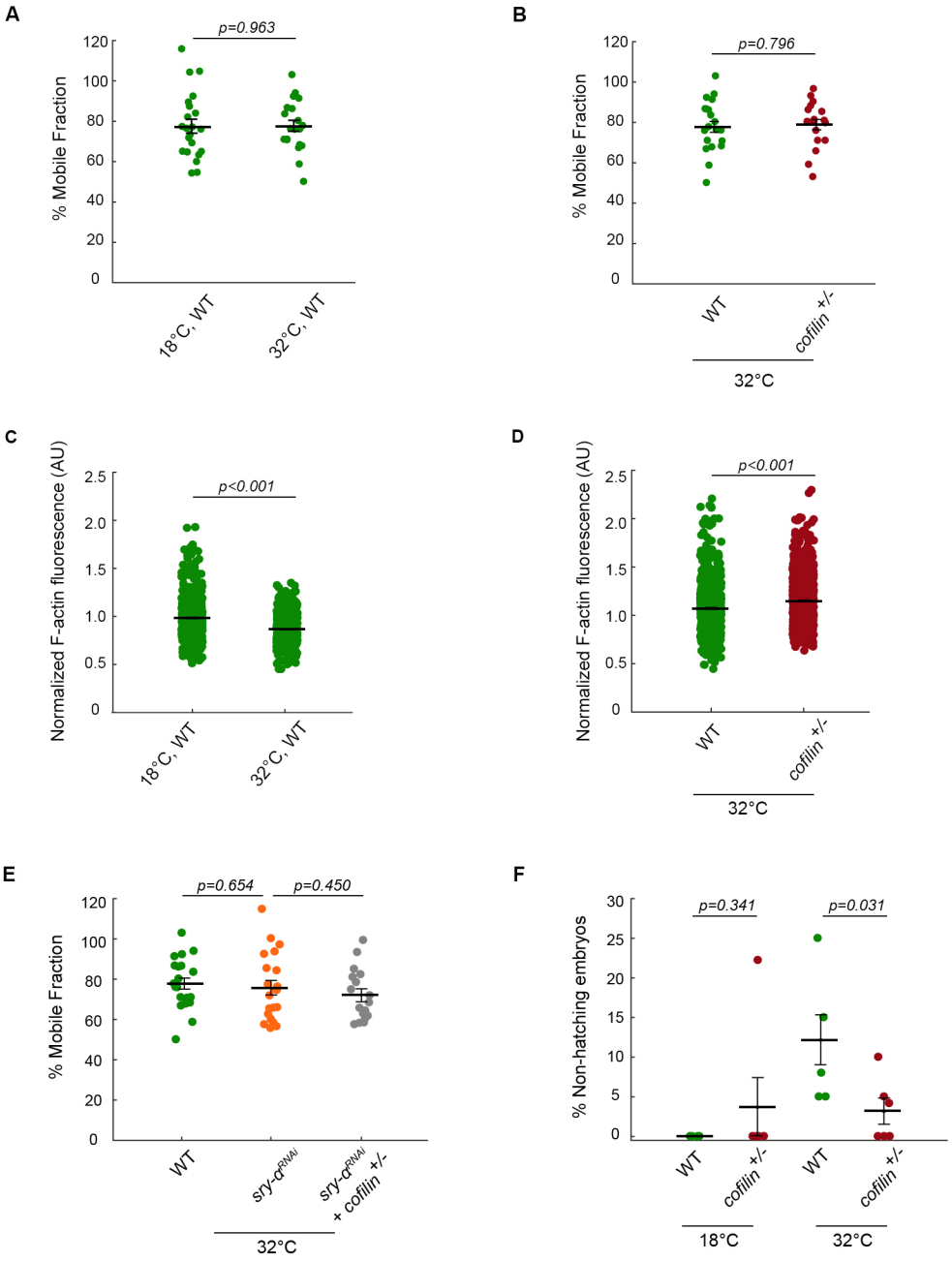

Figure S4. Percent mobile fraction from all FRAP experiments and scatter plots for F-actin quantifications and hatching assays. Related to Figures 3 and 4.

(A) and (B) Percent mobile fraction for furrow tip F-actin in wild-type (WT) or *cofilin*$^{+/-}$ embryos at indicated temperatures (n≥20 embryos per temperature, with 1-3 furrows analyzed per embryo). (C) F-actin levels in furrow tips in WT embryos at indicated temperatures (n≥29 embryos per temperature, with 15 furrows analyzed per embryo). (D) F-actin levels in furrow tips in WT and *cofilin*$^{+/-}$ embryos at 32°C (n≥48 embryos per condition, with 15 furrows analyzed per embryo). (E) Percent mobile fraction for furrow tip F-actin in indicated genotypes at 32°C (n≥20 embryos per temperature, with 1-3 furrows analyzed per embryo). (F) Larval hatching rates for indicated conditions (n≥5 independent experiments, with ≥9 embryos per experiment).

Each point represents one embryo, and horizontal lines are means ± SE for (A), (B), (E) and (F).

Method shown in Figure S3 for (C) and (D).

Each point represents an individual pairwise comparison between all WT embryos and all Histone-GFP embryos, and horizontal lines are means ± SE for (C) and (D).

Student's t-test used to calculate P values in (A)-(F).